JACS
JOURNAL OF THE AMERICAN CHEMICAL SOCIETY

Article

pubs.acs.org/JACS

Band-Gap Energy as a Descriptor of Catalytic Activity for Propene Oxidation over Mixed Metal Oxide Catalysts

Andrew "Bean" Getsoian,[†] Zheng Zhai,[†] and Alexis T. Bell*

Department of Chemical and Biomolecular Engineering The University of California—Berkeley, Berkeley, California 94720-1462, United States

Supporting Information

ABSTRACT: The development of a descriptor or descriptors that can relate the activity of catalysts to their physical properties is a major objective of catalysis research. In this study, we have found that the apparent activation energy for propene oxidation to acrolein over scheelite-structured, multicomponent, mixed metal oxides ($Bi_3FeMo_2O_{12}$, $Bi_2Mo_{2.5}W_{0.5}O_{12}$, and $Bi_{1-x/3}V_{1-x}Mo_xO_4$, where $0 \leq x \leq 1$) correlates with the band gap of the catalyst measured at reaction temperature. We show through theoretical analysis of the energy components comprising the activation energy why the band-gap energy is the primary component dependent on catalyst composition and, hence, why one should expect the activation energy for propene oxidation to correlate with the band-gap energy. We also demonstrate that the change in band-gap energy with composition arises from the interplay between the sizes and energies of the V 3d, Fe 3d, Mo 4d, and W 5d orbitals, which give rise to the lowest unoccupied crystal orbitals. Both the utility of the band-gap energy as a descriptor for catalytic activity and the role of orbital overlap in determining the band gap are likely to be general features in mixed metal oxide oxidation catalysts, enabling the rational design of catalysts with greater activity for oxidation reactions.

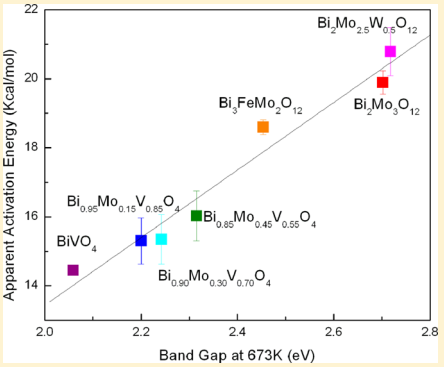

INTRODUCTION

There has been a long-standing interest in the field of catalysis to identify descriptors that relate the observed catalytic activity and selectivity to the physicochemical properties of the catalyst. Having such descriptors should enable the rational design of catalysts with superior catalytic performance by specifying the material properties responsible for such performance and thereby guiding the development of materials with the requisite properties. Insights from theory have proven particularly fruitful in developing such descriptors. For example, Hammer and Nørskov have developed the "d-band model" to describe the adsorption of reactants and intermediates on metal surfaces.[1] This model relates the strength of adsorption of a molecule on a metal surface to the energy of the center of the d band of electronic states in the metal. This model has been refined and extended by a number of researchers[2−6] and has proven useful for predicting the catalytic activity of alloys[7] and metal overlayers[4,8] for a number of reactions, such as CO oxidation, Fischer−Tropsch synthesis, and the electrochemical evolution of oxygen from water.[9]

The success of the d-band model for metals motivates the development of a comparable set of descriptors for the catalytic properties of metal oxides. Metal oxides comprise a large family of catalysts that are used for selective oxidation of alkanes,[10−13] olefins,[14] alcohols,[15,16] and aromatics;[17] selective reduction of nitrogen oxides;[18−20] and oxidation of hydrogen sulfide.[21] Moreover, the most active and selective metal oxides involve successful mixtures of multiple metal oxides (e.g., BiMoO,[22] USbO,[23] VMoNbTeO,[24] VMoO,[25] FeSbO,[26] and FeMoO[27]), the performance of which is typically quite different from that of the component oxides. In mixed oxide systems, both the stoichiometry and the surface structure of the working catalyst may determine the catalytic activity.[28,29] A great deal is known about the chemical reactivity of individual oxide systems,[30,31] and rationales have been proposed for changes in reactivity with composition in the case of a few mixed metal oxide systems.[32−34] In particular, the effect of doping on the catalytic performance of metal oxides has been reviewed in detail by McFarland and Metiu.[35] However, development of a general model by which the effects of composition on catalyst performance in mixed metal oxide systems can be rationalized remains an open challenge.

The desire to establish such a model has led to several alternative approaches. For example, Rossmeisl and co-workers[36] have found that the strength of adsorption of oxygen-containing species O, OH, and OOH on transition-metal oxides is related to the number of outer sphere electrons on the transition-metal center. The authors examined substitution of transition-metal oxides into cubic MO and perovskite AMO_3 structures, where A = Sr^{2+}, Ba^{2+}, La^{3+}, or Y^{3+}, and M is any first row transition metal Sc−Cu. Using density functional theory, linear correlations were found between the strength of adsorption of O, OH, and OOH species and the

Received: May 23, 2014
Published: September 3, 2014

   dx.doi.org/10.1021/ja5051555 | J. Am. Chem. Soc. 2014, 136, 13684−13697

number of electrons occupying d-orbitals on the transition metal to which these species were bound. Such correlations suggest that the d-orbital occupancy reflects the number of electrons available to participate in bonding between the metal center and the adsorbate. This model represents a significant step toward understanding the reactivity of oxygen species on transition-metal oxide surfaces.

A further significant step toward relating the reactivity of mixed metal oxides to fundamental physicochemical properties has been taken by Morgan and his collaborators.[37] In a study also focusing on multicomponent perovskite-structured oxides, they demonstrate that oxygen vacancy formation energy closely correlates to catalytic activity toward solid oxide fuel cell autothermal re-forming reactions. The relevance to catalysis of oxygen vacancy formation energy arises from the importance of oxygen diffusion through the perovskite lattice during autothermal re-forming. The authors further show that the oxygen vacancy formation energy can be directly related to the oxygen p-band center energy for a wide range of solid oxide compositions, thus enabling catalytic activity to be predicted from a first-principles descriptor. However, the authors also show that this descriptor fails for the composition family $(La,Sr)MnO_3$, for which bulk oxygen diffusion is known not to be rate-determining. Thus, there remains a need for a model applicable to oxidation reactions over mixed metal oxides in which bulk oxygen diffusion does not determine catalytic rates.

In attempting to develop new models in one field, it is often useful to consider models that have already proven successful in other fields. A notable example of such an attempt directed at providing a set of descriptors for metal oxide catalysts has been reported by Bordes-Richard and by Courtine and co-workers.[38−40] These researchers used the concept of "optical basicity," first developed by Duffy and Ingram[41] in the 1970s for rationalizing the glass-forming properties of main group oxides, and adapted it to catalysis. They showed that for a variety of catalysts, the optical basicity of the catalyst correlates with the product selectivity for the oxidation reactions of alkanes, alkenes, and alcohols. However, there are problems in the general application of this method to metal oxide catalysts. Optical basicity, Λ, is derived by experimentally measuring the energy of the 6s → 6p excitation on Pb^{2+} or Bi^{3+} ions doped in low concentration into the oxide of interest. Unfortunately, this measurement cannot be conducted in transition-metal oxides, as light absorption from the transition metal overwhelms the signal from the probe cation, necessitating the use of scaling relationships to determine optical basicity values. Unfortunately, major contradictions arise in such scaling relationships for catalytically important ions such as V^{5+}: the optical basicity assigned using band-gap correlations[42] is $\Lambda = 1.04$ (more basic than Ca^{2+}), using the iono-covalent parameter[43] yields $\Lambda = 0.63-0.69$ (acid−base properties similar to Al^{3+}), and using Brønsted acidity[44] gives $\Lambda = 0.49$ (as acidic as P^{5+}). The value of optical basicity is also likely limited to systems in which acid−base properties are important for catalysis. Therefore, the concept of optical basicity is not applicable to systems such as bismuth molybdates, which are known to oxidize olefins via a radical mechanism.

For catalysis over transition-metal sulfides, the metal−sulfur (M−S) bond strength has been proposed as a descriptor for catalytic activity.[45] In a series of studies,[46−49] Toulhoat, Raybaud, and their collaborators demonstrate the utility of this descriptor in accounting for both adsorption and activation enthalpies in catalytic hydrogenation, hydrogenolysis, and hydrodesulfurization reactions. However, analysis by Wachs and co-workers has determined that an analogous relationship between metal−oxygen bond strength and the activities of transition-metal oxides toward oxidation reactions does not exist.[50] That such a descriptor succeeds for sulfides but fails for oxides may be a consequence of structural differences between oxide and sulfide phases: the surfaces of transition-metal oxides often contain metal−oxygen bonds with significant double bond character, with the degree of double bond character differing for different surface terminations and between surface and bulk. By contrast, transition-metal sulfide surfaces typically contain metal−sulfur single bonds, the character of which differs much less between surface and bulk. The bulk M−S bond strength is therefore more relevant to the description of bond-breaking and bond-forming processes occurring during catalysis on transition-metal sulfide surfaces than the bulk M−O bond strength is to such processes occurring on the surfaces of transition-metal oxides.

Idress and Seebauer[51] have proposed that the catalytic reactivity of oxides is related to the polarizability of oxygen. They have shown that the rates of ethanol dehydrogenation to acetaldehyde and of 2-propanol oxidation to acetone over a series of binary oxides correlate very closely with the polarizability of the oxygen atoms in each oxide lattice. A similar trend was found for the rate of the Tishchenko reaction over alkali earth oxides. Since lattice oxygen is involved in the rate-determining steps of these reactions, it is reasonable to connect catalyst reactivity to a physical characteristic of the reacting oxygen atoms. However, this approach has not been extended to mixed metal oxide systems, so it is not possible to comment on the utility of oxygen polarizability as a predictive descriptor for rational catalyst design.

Another model that has shown substantial explanatory power is the band-edge model widely used in semiconductor physics and photocatalysis. In the design of semiconductor systems such as light-harvesting diodes, the band-edge model provides key information about the electronic properties produced by the interface between materials of differing composition.[52] In photocatalysis, the same model provides information about the electronic properties (and therefore catalytic properties) of the interface between a semiconducting catalyst and an aqueous reactant.[53] Whether a material is a potentially suitable catalyst for photo(electro)chemical production of hydrogen, for example, can be determined directly from an inspection of conduction band-edge energy of the material.[54,55]

In attempting to identify descriptors of catalytic activity for mixed metal oxide oxidation catalysts, it is helpful to recognize that the chemical properties of both the metal and oxygen centers will contribute to the catalytic performance of the oxide. In particular, oxidation of hydrocarbons is often understood to proceed via the interaction of surface oxygen atoms with carbon or hydrogen atoms of adsorbed reactants, in conjunction with electron transfer from the adsorbate to reducible transition-metal centers in the catalyst. A simple descriptor that captures both the nature of the reactive oxygen centers and the tendency of adjacent transition-metal centers to gain electron density is the ligand-to-metal charge transfer (LMCT) excitation energy. For metal oxides containing transition-metal centers in their highest oxidation states, the LMCT excitation energy typically corresponds to the band-gap energy. In chemical terms, the band-gap energy can be thought of as the energy difference between the highest occupied crystal orbital (which is typically oxygen-centered) and the lowest unoccupied crystal orbital

dx.doi.org/10.1021/ja5051555 | J. Am. Chem. Soc. 2014, 136, 13684−13697

(which is transition-metal-centered). The band-gap energy therefore contains information about the frontier molecular orbitals in a crystalline material. The relative energies of frontier molecular orbitals have long been used to rationalize reactivity in molecular systems.[56,57] The character of the frontier crystal orbitals is also an important descriptor for the catalytic activity of transition-metal sulfides toward hydrodesulfurization reactions.[58] It is therefore of interest to determine whether the energy difference between frontier crystal orbitals in a mixed metal oxide can be used as a descriptor of catalytic activity.

The objective of the present work is to determine the extent to which it is possible to explain trends in activation energy with composition for a family of oxidation catalysts in terms of the LMCT excitation energy or band gap. To decouple differences in observed band gap due to composition from differences due to changes in crystal structure, only catalysts with the scheelite crystal structure were considered. In particular, attention was focused on $Bi_3FeMo_2O_{12}$, $Bi_2Mo_{2.5}W_{0.5}O_{12}$, and solid solutions of composition $Bi_{1-x/3}V_{1-x}Mo_xO_4$, where $0 \leq x \leq 1$. The reaction chosen for investigation was the oxidation of propene to acrolein because the mechanism and kinetics of this reaction have been investigated extensively over $Bi_2Mo_3O_{12}$ and related oxides.[59−65] The principal findings are that the rate of the reaction is first-order in propene and zero-order in oxygen. Consistent with these kinetics, H/D isotopic labeling indicates that the rate-limiting step is the cleavage of one C−H bond in the methyl group of propene.[59,60] ^{13}C labeling studies have shown that this step produces a symmetric allyl radical.[61] The initial C−H bond cleavage and the subsequent insertion of oxygen to produce acrolein involve oxygen in the catalyst lattice, indicating that propene oxidation proceeds via a Mars−van Krevelen mechanism.[62,66] Kinetics identical to those for $Bi_2Mo_3O_{12}$ have been reported for other scheelites with the composition $Bi_{1-x/3}V_{1-x}Mo_xO_4$.[67] That work has also demonstrated that in contrast to earlier proposals, only Mo and V cations undergo reduction and oxidation, but not Bi. The mechanism of propene oxidation proposed for $Bi_2Mo_3O_{12}$ has also been the subject of several theoretical studies.[68−74] Detailed density functional theory calculations performed within our group have revealed that the lone pair of Bi interacts with an equatorial Mo=O bond, thereby making the O atom in this bond significantly more active than Mo−O−Bi or axial Mo=O bonds.[73,74] A similar conclusion regarding the active site for propene oxidation on $Bi_2Mo_3O_{12}$ had previously been reached by the Goddard group in a modeling study employing the ReaxFF reactive force field.[72]

As stated above, the objective of the present work is to develop a first-principles descriptor explaining the composition dependence of activation energy for propene oxidation over mixed metal oxides. In order to develop a complete understanding of the factors determining observed reaction rates, descriptors accounting for contributions to the pre-exponential factor must also be developed. Such contributions include the entropy of adsorption of propene on the catalyst surface, the intrinsic activation entropy for C−H bond activation at the active site(s), and the number and distribution of active sites. Evaluation of these contributions is, however, beyond the scope of the present work.

METHODS

Experimental Methods. Catalysts with the generic composition $Bi_{1-x/3}V_{1-x}Mo_xO_4$ were prepared by the complexation procedure using citric acid.[67] Citric acid was added to aqueous solutions of the metal precursors bismuth(III) nitrate pentahydrate, ammonium molybdate tetrahydrate, and ammonium metavanadate. Solutions were then mixed in the atomic ratios of Bi:V:Mo = $(1 - x/3):(1 - x):x$, (x = 0 to 1.0). To prepare $Bi_2Mo_{2.5}W_{0.5}O_{12}$, ammonium molybdate tetrahydrate, bismuth(III) nitrate pentahydrate, and ammonium tungstate, with citric acid, were mixed at the atomic ratios of Bi:Mo:W = 2:2.5:0.5. $Bi_3FeMo_2O_{12}$ was prepared by mixing ammonium molybdate tetrahydrate, bismuth(III) nitrate pentahydrate, and iron(III) nitrate, with citric acid, in the atomic ratios of Bi:Mo:Fe = 3:2:1. Each of the resulting solution was dried at 60 °C for about 24 h in air to form a gel. The gel was then dried further at 120 °C and calcined in flowing air at 600 °C for 6 h. The phase purity of the catalysts formed was confirmed by X-ray diffraction (see the Supporting Information).

Diffuse reflectance UV−vis−NIR spectra were acquired using a Fischer Scientific EVO 300 spectrometer equipped with a Praying Mantis reflectance chamber and an in situ high-pressure cell (Harrick Scientific, Inc.), fitted with quartz windows. Spectra were referenced to the diffuse reflectance spectrum of a Teflon reference tile. The procedure used to extract band-gap energies from absorption edge data is discussed in the Supporting Information.

XANES scans were taken at the Mo and V K edges and Bi L3 edge at beamline 10-BM at the Advanced Photon Source at Argonne National Laboratory. Experimental details are provided in the Supporting Information.

Theoretical Methods. Bulk and slab density functional theory calculations were carried out using VASP[75] 5.3.3. Projector augmented wave cores[76,77] containing kinetic energy density information were used to represent core electrons, while plane wave basis sets[78] with cutoff energies of 450 eV were used to represent valence electrons. Electron exchange and correlation was modeled using the M06-L density functional.[79,80] Successful use of this functional within VASP requires nondefault values of several input parameters; these are provided in the Supporting Information.

Crystal structures taken from the literature[81−83] were used for $BiVO_4$ (minimal unit cell $Bi_4V_4O_{16}$), $Bi_2Mo_3O_{12}$ (minimal unit cell $Bi_8Mo_{12}O_{48}$), and $Bi_3FeMo_2O_{12}$ (minimal unit cell $Bi_{12}Fe_4Mo_8O_{48}$), and lattice constants and atomic positions were allowed to relax to minimize the total energy within the M06-L functional. Relaxed lattice constants differed from experimental values by <0.5% in all cases. To model the $Bi_{1-x/3}V_{1-x}Mo_xO_4$ phase[34] with an intermediate value of x, the smallest possible mixed vanadate−molybdate structure was constructed. This minimal model, of formula $Bi_7V_5Mo_3O_{12}$, was built from a $Bi_8V_8O_{32}$ supercell by substitution of three V sites by Mo and removal of one Bi to form a charge-compensating cation vacancy. $Bi_2Mo_{2.5}W_{0.5}O_{12}$ was modeled by replacing two molybdenum atoms in a $Bi_8Mo_{12}O_{48}$ unit cell with W atoms to yield a model of stoichiometry $Bi_8W_2Mo_{10}O_{48}$. Details of the construction of these models can be found in the Supporting Information. While these minimal models cannot fully account for the experimentally observed random substitution of V or W for Mo, they nevertheless provide useful insights into the electronic consequences of substitution at transition-metal centers.

Band structures (crystal orbitals) were obtained by calculating the site projected density of states. By default, the zero of energy in a VASP-generated density of states calculation is the energy of the highest occupied state. In this work, it was desirable to instead choose the reference zero energy to be the energy of the vacuum state (i.e., the energy of electrons and nuclei separated at infinity). With this choice of reference state, Koopmans' theorem[84] states that the energy of the highest occupied state is an approximation of the first ionization energy (IE) of the material, and the energy of the lowest unoccupied state is an approximation of the electron affinity (EA). The procedure used to adjust the zero energy in density of states plots is described in the Supporting Information.

RESULTS AND DISCUSSION

Kinetics of Propene Oxidation. The kinetics of propene oxidation to acrolein were measured in a fixed bed reactor

dx.doi.org/10.1021/ja5051555 | J. Am. Chem. Soc. 2014, 136, 13684−13697

operating at atmospheric pressure and temperatures between 633 and 713 K. Conversion was maintained below 1% in order to minimize the effects of secondary reactions. For all of the materials investigated, the selectivity to acrolein was greater than 65%. Table 1 lists the reaction orders in propene and

Table 1. Rate Parameters for Propene Oxidation to Acrolein

	rate = $k_{app}P_{C_3H_6}{}^{m}P_{O_2}{}^{n}$ = $A_{app}\exp(-E_{app}/RT)P_{C_3H_6}{}^{m}P_{O_2}{}^{n}$				
	$k_{app}{}^{a}$	$A_{app}{}^{b}$	$E_{app}{}^{c}$	m	n
$BiVO_4$	1.74	9	14.5	1.0	0.0
$Bi_{0.95}V_{0.85}Mo_{0.15}O_4$	2.36	22	15.3	1.0	0.0
$Bi_{0.90}V_{0.70}Mo_{0.30}O_4$	3.28	30	15.3	1.0	0.0
$Bi_{0.85}V_{0.55}Mo_{0.45}O_4$	3.54	55	16.0	0.9	0.1
$Bi_3FeMo_2O_{12}$	0.36	39	18.6	1.0	0.0
$Bi_2Mo_3O_{12}$	0.67	195	19.9	1.0	0.0
$Bi_2Mo_{2.5}W_{0.5}O_{12}$	0.38	216	20.8	1.0	0.0

[a]Apparent rate constant at 673 K, in $\times 10^{-5}$ mol/(min m^2 cat. atm). [b]Apparent pre-exponential constant in $\times 10^{-4}$ mol/(min m^2 cat. atm). [c]Apparent activation energy in kcal/mol

oxygen, apparent rate constant at 673 K, the apparent activation energy, and the apparent pre-exponential factor for each catalyst. For the temperature range chosen, the rate of acrolein formation is essentially first-order in propene and zero-order in oxygen (reaction order plots are shown in the Supporting Information). The latter result indicates that under the conditions chosen, the catalyst is saturated with oxygen. The production rate of acrolein does not change when the conversion increases, demonstrating no inhibition by acrolein under experimentally relevant low-conversion conditions. (Plots are shown in the Supporting Information).

UV–Vis–NIR and XANES Spectroscopy. Figure 1 shows the absorption edges for a series of solid solutions having the

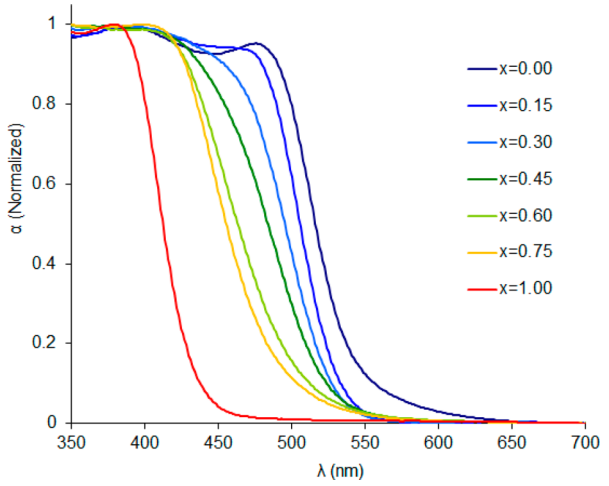

Figure 1. Diffuse reflectance UV–visible absorption spectra for catalysts with composition $Bi_{1-x/3}V_{1-x}Mo_xO_4$.

stoichiometry $Bi_{1-x/3}V_{1-x}Mo_xO_4$. The absorption edges determined for bismuth vanadate and bismuth molybdate are consistent with those reported previously.[85,86] Each material exhibits only a single absorption edge, with the position of the edge shifting monotonically with the relative proportions of vanadium and molybdenum. This result indicates that vanadate and molybdate ions are not electronically independent, but rather, the electronic properties of the mixed metal oxide depend upon the relative proportions of vanadate and molybdate ions present in the material. By contrast, a physical mixture of bismuth vanadate and bismuth molybdate exhibits two separate absorption edges (see Supporting Information).

The diffuse reflectance spectra of $Bi_3FeMo_2O_{12}$ and $Bi_2Mo_{2.5}W_{0.5}O_{12}$ are shown in Figure 2. The absorption edge

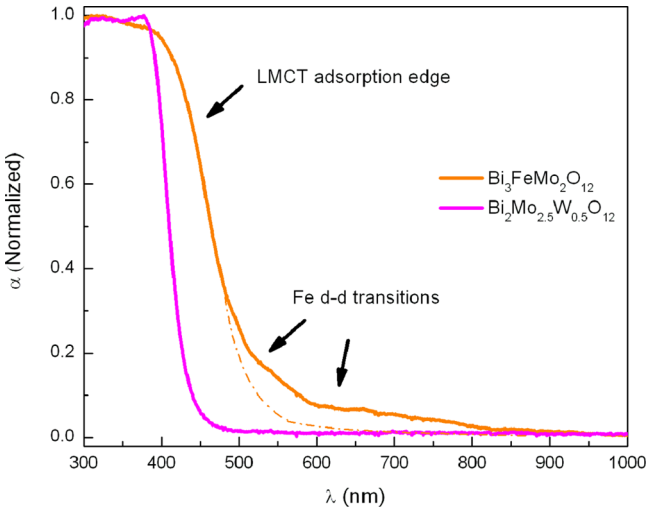

Figure 2. Diffuse reflectance UV–visible absorption spectrum of $Bi_3FeMo_2O_{12}$ and $Bi_2Mo_{2.5}W_{0.5}O_{12}$. For $Bi_3FeMo_2O_{12}$, labels mark the principal LMCT absorption edge and the pre-edge absorption features arising from occupied Fe 3d orbitals.

of $Bi_3FeMo_2O_{12}$ is lower in energy than that of $Bi_2Mo_3O_{12}$, indicating that Fe substitution, like V substitution, reduces the band-gap energy. The spectrum of $Bi_3FeMo_2O_{12}$ also exhibits absorption features at energies below the edge, attributable to the presence of occupied d-orbitals on Fe^{3+} ions. These absorption features may arise from d–d excitations on individual Fe atoms (which, however, are both spin and Laporte forbidden for the d^5 high-spin tetrahedral Fe^{3+} ion), or they may arise from the charge transfer excitation process $2Fe^{3+} \rightarrow Fe^{2+} + Fe^{4+}$ between neighboring Fe ions. In either case, the spectrum in Figure 2 indicates that (1) the band gap in $Bi_3FeMo_2O_{12}$ is lowered relative to that in $Bi_2Mo_3O_{12}$, presumably via coupling between Mo and Fe electronic states, and (2) there exist additional Fe electronic states in $Bi_3FeMo_2O_{12}$ which are not coupled to Mo states and which give rise to additional features in the absorption spectrum. As discussed below, both points 1 and 2 are relevant to understanding the impact of Fe substitution on the catalytic performance of bismuth molybdate. The diffuse reflectance UV–visible spectrum of $Bi_2Mo_{2.5}W_{0.5}O_{12}$ closely resembles that of $Bi_2Mo_3O_{12}$.

Heating bismuth molybdate-based catalysts in nonreducing atmospheres (e.g., helium or air) caused a shift in the absorption edge to lower energies (see Supporting Information). This shift is attributable to strong coupling between electronic states and lattice vibrations (phonons), together with a smaller effect due to thermal expansion of the lattice. The relationship between band gap and temperature is almost perfectly linear across the temperature range studied (298–713 K), as expected from theory.[87,88] Thermal effects on band gaps are qualitatively similar across all catalysts studied, with the magnitude of the decrease in band gap varying from 0.1–0.2 eV

dx.doi.org/10.1021/ja5051555 | J. Am. Chem. Soc. 2014, 136, 13684–13697

upon heating from ambient conditions to 713 K, depending on catalyst composition. The band gaps for all materials studied, as measured at 673 K, are given in Table 2.

Table 2. Band-Gap Energies (eV) Measured at 298 and 673 K and Calculated

	E_G(298K)	E_G(673K)	E_G(DFT)
$BiVO_4$	2.34	2.06	2.28
$Bi_{0.950}V_{0.850}Mo_{0.150}O_4$	2.42	2.20	[b]
$Bi_{0.900}V_{0.700}Mo_{0.300}O_4$	2.43	2.24	[b]
$Bi_{0.875}V_{0.625}Mo_{0.375}O_4$	[a]	[a]	2.38
$Bi_{0.850}V_{0.550}Mo_{0.450}O_4$	2.47	2.32	[b]
$Bi_3FeMo_2O_{12}$	2.57	2.45	2.64
$Bi_2Mo_3O_{12}$	2.97	2.70	2.80
$Bi_2Mo_{2.5}W_{0.5}O_{12}$	2.99	2.72	2.84

[a]Not measured experimentally. [b]Not calculated within DFT.

Heating $Bi_{1-x/3}V_{1-x}Mo_xO_4$ at 673 K in an oxidizing atmosphere and then exposing it to 20% propene in helium caused a time-dependent shift in the baseline UV−vis absorbance (e.g., the absorbance at all energies below the edge), indicating reduction of the catalyst (see Supporting Information). This observation is consistent with a Mars−van Krevelen mechanism in which propene is oxidized by lattice oxygen, leading to reduction of the catalyst. In fact, the initial rate of catalyst reduction determined from UV−vis data is proportional to the measured rate of propene oxidation. However, these data do not reveal which element(s) undergo reduction. For this reason, in situ XANES experiments were carried out in order to determine the extent to which Bi, Mo, and V are reduced by propene and whether reduction of all elements occurs concurrently or sequentially.

Figures 3 and 4 show in situ XANES spectra collected during reduction of $Bi_{0.85}V_{0.55}Mo_{0.45}O_4$ at 713 K in propene flowing at 100 mL/min. Reduction was initiated after pretreatment in air at 713 K to ensure a fully oxidized initial state prior to reduction. While experimental details preclude rigorous investigation of reduction kinetics (see Supporting Information), observation of the qualitative features of the reduction process is sufficient for the present investigation. Under reducing conditions, a decrease in the pre-edge peak intensity and an edge shift to lower energy begin immediately upon exposure to reducing conditions, as seen in Figure 3a. Both changes are consistent with reduction of vanadium. Figure 3b shows that the initial pre-edge peak height and edge position are consistent with tetrahedrally coordinated V^{5+}, as expected from the stoichiometry and known crystal structure of $Bi_{1-x/3}V_{1-x}Mo_xO_4$. After 5 min exposure to propene, reduction is essentially complete. Figure 3c shows that after reduction, the V K edge position is consistent with that for V^{4+}; however, the pre-edge peak height is much larger than that for VO_2. The pre-edge feature arises from a 1s → 3d transition, which is formally prohibited by the selection rule for photon absorption ($\Delta L = \pm 1$). It is therefore only observed for coordination environments in which mixing of 3d and 4p orbitals is allowed by symmetry. Such mixing is strong in tetrahedral coordination such as that in NH_4VO_3 and the as-prepared $Bi_{0.85}V_{0.55}Mo_{0.45}O_4$, but becomes weaker as the coordination environment becomes more octahedral. Vanadium in VO_2 sits in a distorted octahedral environment with weak 3d−4p mixing, resulting in a weak pre-edge peak. The much greater pre-edge peak height in the reduced x = 0.45 catalyst indicates that the vanadium centers in the reduced catalyst retain their nearly tetrahedral coordination.

The Mo K edge XANES shown in Figure 4a show trends in qualitative agreement with those seen in the V K edge XANES

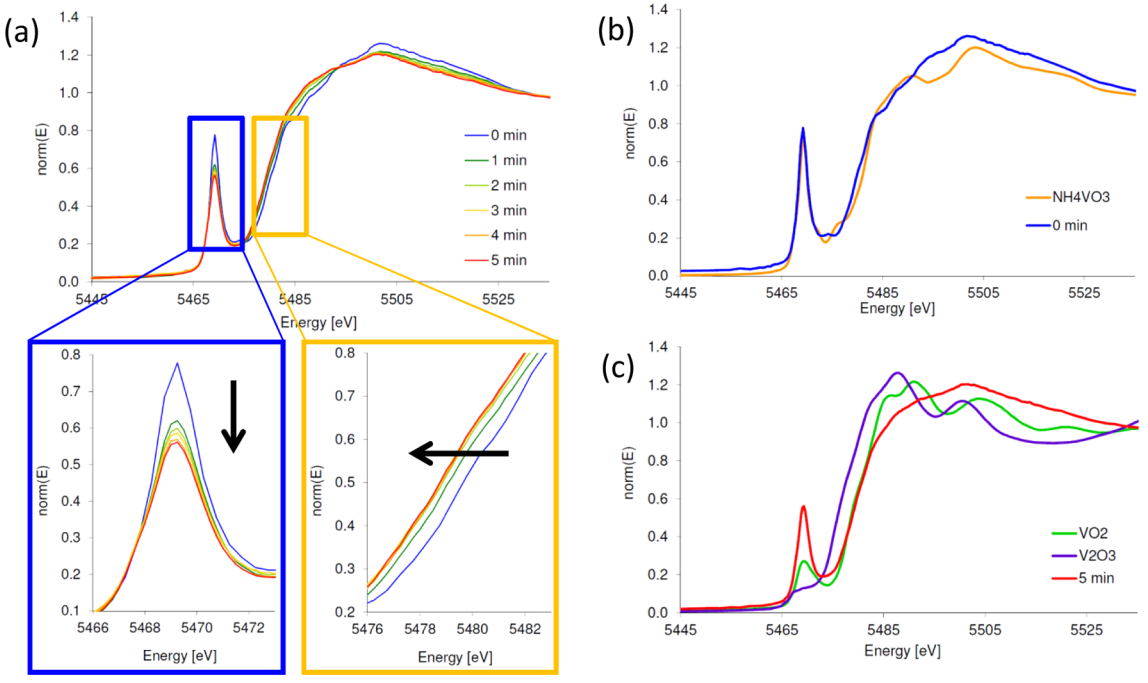

Figure 3. (a) Vanadium K edge XANES spectra for $Bi_{0.85}V_{0.55}Mo_{0.45}O_4$ (x = 0.45) as a function of time of exposure to propene (99%, 100 mL/min) at 713 K. The decrease in pre-edge peak height and red-shift in edge energy have been magnified to illustrate spectral changes occurring during reduction. (b) Spectra of fully oxidized $Bi_{0.85}V_{0.55}Mo_{0.45}O_4$ and a reference compound, NH_4VO_3, containing tetrahedral V^{5+}. (c) Comparsion of the reduced catalyst to reference compounds containing pseudo-octahedral V^{4+} (VO_2) and V^{3+} (V_2O_3).

dx.doi.org/10.1021/ja5051555 | J. Am. Chem. Soc. 2014, 136, 13684−13697

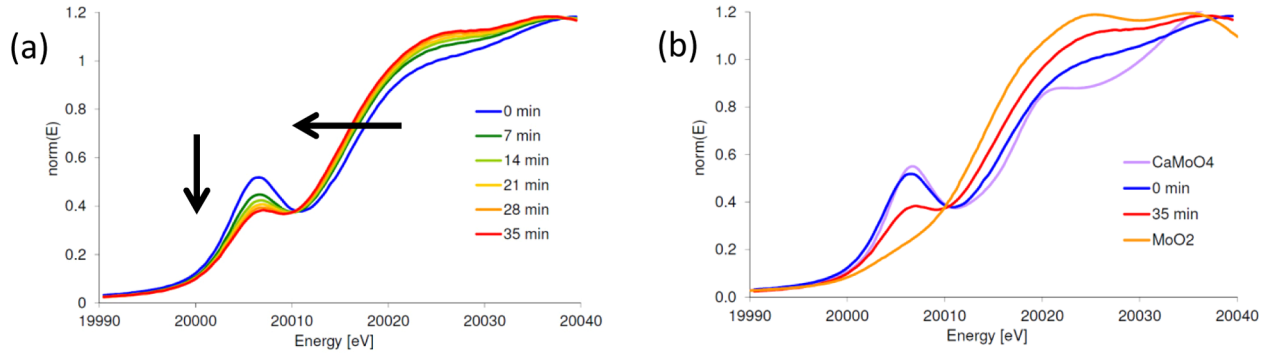

Figure 4. (a) Molybdenum K edge XANES spectra of $Bi_{0.85}V_{0.55}Mo_{0.45}O_4$ as a function of time of exposure to propene (99%, 100 mL/min) at 713 K. (b) Comparison of the oxidized and reduced catalysts to reference compounds containing tetrahedral Mo^{6+} ($CaMoO_4$) and pseudo-octahedral Mo^{4+} (MoO_2).

in Figure 3a: a decrease in pre-edge peak intensity and a shift of the absorption edge to lower energies. Although the reduction conditions (100 mL/min 99% propene at 713 K) are the same as in the vanadium case, the catalyst loading required to obtain a good XANES signal is different, resulting in a different time scale for reduction. Nevertheless, these results show that Mo reduction begins immediately upon exposure to reducing conditions, identical to the case for vanadium. The XANES spectrum of the as-prepared $Bi_{0.85}V_{0.55}Mo_{0.45}O_4$ contains tetrahedrally coordinated Mo^{6+} sites similar to those present in $CaMoO_4$. Exposure to reducing conditions leads to a pre-edge feature height and an edge position midway between those expected for Mo^{6+} and Mo^{4+}. This observation is consistent with formation of either Mo^{5+} sites or with a mixture of both Mo^{4+} and Mo^{6+} sites. Investigations using XPS and EPR have detected both Mo^{4+} and Mo^{5+} in reduced bismuth molybdate,[89−91] and DFT calculations suggest that both Mo^{4+} and Mo^{5+} are formed during reduction of bismuth molybdate by propene. No stoichiometric Mo^{5+} oxide phase is known, and in mixed-valence oxides such as Mo_4O_{11}, extensive delocalization of Mo d electrons[92,93] precludes the assignment of integral oxidation states to individual molybdenum centers. While the relative concentrations of formally Mo^{6+}, Mo^{5+}, and Mo^{4+} sites cannot be assessed from the data in Figure 4, it is evident that reduction of molybdenum begins immediately upon exposure to propene. It can therefore be concluded that during reduction of $Bi_{0.85}V_{0.55}Mo_{0.45}O_4$, vanadium and molybdenum undergo reduction simultaneously. This conclusion is extended to other catalysts with the composition $Bi_{1-x/3}V_{1-x}Mo_xO_4$ based on our earlier work,[67] which showed that exposure of such materials to 100 mL/min of 99% propene at 713 K for 24 h resulted in the reduction of V^{5+} to V^{4+} and Mo^{6+} to Mo^{4+}. That work also demonstrated that Bi^{3+} does not undergo reduction.

Band-Gap Energy as a Descriptor of Activation Energy. Figure 5 shows the apparent activation energy for each catalyst plotted as a function of the band-gap energy measured at 673 K. This relationship can be understood by relating the band gap to the elementary processes involved in attaining the transition state for the rate-limiting step of propene oxidation, the step which involves cleavage of a C−H bond in the methyl group of the reactant.

The band gap in a semiconductor separates the highest occupied and lowest unoccupied crystal orbitals. In bismuth molybdate, both the highest occupied and lowest unoccupied crystal orbitals are centered on the molybdate ions: the highest

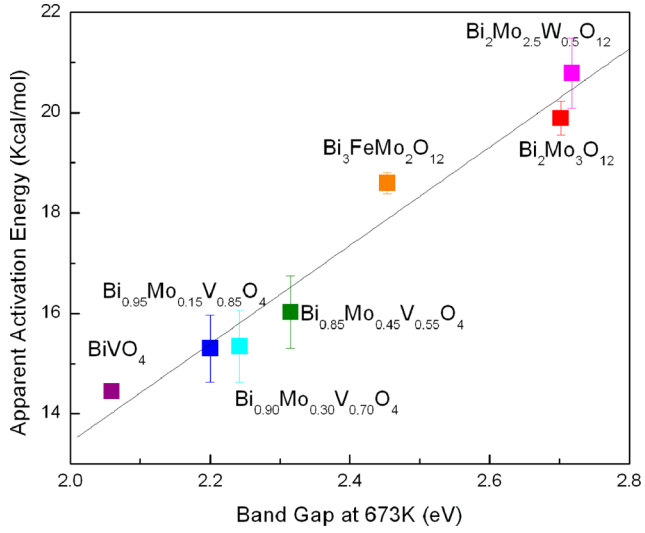

Figure 5. Apparent activation energies for oxidation of propene to acrolein over substituted bismuth molybdates.

occupied states consist of O 2p lone pair orbitals of local t_1 symmetry, while the lowest unoccupied states consist of the Mo 4d orbitals of local e symmetry (the d_{z^2} and $d_{x^2-y^2}$). The band gap thus arises from a ligand-to-metal charge transfer (LMCT) process in which an excited electron is formally transferred from oxygen to molybdenum. This process can be represented as $Mo^{6+}{=}O^{2-} \rightarrow Mo^{5+}{-}O^{1-}$ and gives rise to the absorbance maximum near 380 nm for $Bi_2Mo_3O_{12}$ seen in Figure 1.

Likewise, for vanadate ions, the highest occupied states consist of O 2p lone pair orbitals of local t_1 symmetry, while the lowest unoccupied states consist of the V 3d orbitals of local e symmetry. The band gap in $BiVO_4$ thus arises from an LMCT process that can be written schematically as $V^{5+}{=}O^{2-} \rightarrow V^{4+}{-}O^{1-}$. The V 3d(e) ← O 2p($t_1$) LMCT excitation in $BiVO_4$ gives rise to the absorbance maximum near 475 nm in Figure 1. (A second higher energy absorbance maximum arising from the V 3d(t_2) ← O 2p(t_1) excitation is also visible near 390 nm.) As shown in Scheme 1, both LMCT excitation processes can be depicted as M═O → •M—O•.

Density functional theory calculations of propene activation over $Bi_2Mo_3O_{12}$ have been reported previously,[69−74] and DFT calculations of the activation barrier for propene activation over $BiVO_4$ are given in the Supporting Information. This work provides a generic picture of the transition state for C−H activation over a surface M═O structure (M = Mo, V). As

dx.doi.org/10.1021/ja5051555 | J. Am. Chem. Soc. 2014, 136, 13684−13697

Scheme 1. Ligand-to-Metal Charge Transfer Excitation

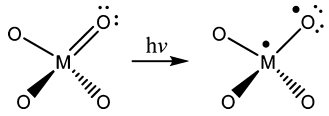

shown in Figure 6, the transition state for C−H bond activation involves three simultaneous processes: dissociation of a C−H bond, formation of an O−H bond, and elongation and rehybridization of an M═O double bond to yield an M−O single bond. The sum of these three processes can be written as $M^{n+}{=}O^{2-} + C_3H_6 \rightarrow \bullet M^{(n-1)+}{-}OH + \bullet C_3H_5$.

Figure 7 demonstrates how the contributions from each of the three components to the overall reaction barrier can be represented in terms of a Born−Haber cycle. The bond dissociation energy for a C−H bond in the methyl group of propene is 88.2 kcal/mol.[94] The remaining contributions are summarized in Table 3. The H bond formation energy E_{OH} was determined by calculating the energy released by the attachment of an H radical to •M—O•. A value of ΔE_{OH} of 117.9 kcal/mol was obtained for M = Mo and 115.8 kcal/mol for M = V, suggesting that the O−H bond energy does not depend strongly on the identity of the nearest neighbor to oxygen. For comparison, the dissociation energy for the first O−H bond in water is 117.59 kcal/mol.[95]

The value of $E_{stretch}$ was determined by subtracting the energy of the model catalyst surface with the active site M═O bond at the M−O bond distance of the initial state for C−H bond activation (1.60 Å for V═O, 1.74 Å for Mo═O; see Supporting Information) from the energy of the model catalyst surface with the active site M═O bond stretched to the M−O bond distance in the M−OH final state (1.74 Å for V−O, 2.00 Å for Mo−O). Again, the values of $E_{stretch}$ are similar for $BiVO_4$ and $Bi_2Mo_3O_{12}$. Remarkably, the 2.1 kcal/mol greater $E_{stretch}$ required to elongate the Mo═O bond is exactly matched by a 2.1 kcal/mol greater Mo−OH bond strength. This cancelation may indicate a compensation effect whereby the M−O bond will undergo a greater (more energetically costly) deformation in order to form a stronger M−OH bond.

E_{hyb} was calculated as the difference in energy between singlet M═O and triplet •M—O• orbital configurations for the M−O bond at the final state (M−OH) geometry (but with no H atom attached) and reflects only the energy required to rearrange electron density within the M−O bond.[96] As seen in Table 3, the largest difference between $BiVO_4$ and $Bi_2Mo_3O_{12}$ occurs for the E_{hyb} term. Furthermore, the compensation between $E_{stretch}$ and E_{OH} eliminates the composition dependence of the sum $E_{stretch} + E_{OH}$; as a result, almost the entire

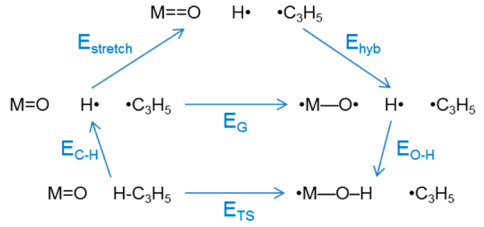

Figure 7. Born−Haber cycle decomposition of the transition-state energy (E_{TS}) into contributions from C−H bond breaking (E_{C-H}), M═O bond elongation ($E_{stretch}$), M═O bond rehybridization (E_{hyb}), and O−H bond formation (E_{O-H}).

Table 3. Measured and Calculated Band-Gap Energies (E_G, in eV) and Calculated Values for E_{strech}, E_{hyb}, and E_{OH} (in kcal/mol)

	$BiVO_4$	$Bi_2Mo_3O_{12}$
E_G from DRUVS at 673 K	2.06	2.70
E_G from DFT	2.28	2.80
$E_{stretch}$	20.9	23.0
E_{hyb}	30.1	39.0
E_{OH}	−115.8	−117.9

difference in E_{TS} between $BiVO_4$ and $Bi_2Mo_3O_{12}$ is due to the E_{hyb} term. Importantly, the metal−oxygen bond reorganization energy described by E_{hyb}—transfer of an electron from a nonbonding oxygen 2p-derived state into a metal d-derived state with π^*(M═O) antibonding character—corresponds to an LMCT excitation. Both the M−O bond reorganization taking place at the C−H bond activation transition state and the LMCT excitation that gives rise to the band gap involve the M═O → •M—O• redistribution of electron density depicted in Scheme 1. It is for this reason that the band-gap energy emerges as a descriptor of catalytic activity.

The excited state generated in an LMCT excitation has a sufficiently long enough lifetime to undergo vibrational relaxation. This is the reason why the band-gap energy is sensitive to temperature. Therefore, the band-gap energy should contain contributions from both geometric and electronic rearrangement, and we expect $E_G \approx E_{stretch} + E_{hyb}$. Indeed, the sum $E_{stretch} + E_{hyb}$ = 51 kcal/mol for $BiVO_4$ and 62 kcal/mol for $Bi_2Mo_3O_{12}$ nearly equal to the band-gap energies of 2.28 eV = 52.6 kcal/mol for $BiVO_4$ and 2.80 eV = 64.6 kcal/mol for $Bi_2Mo_3O_{12}$ determined from density of states calculations. The close agreement between E_G values obtained from two different calculations—a Born−Haber cycle describing changes to the catalyst occurring during C−H bond activation and a density of states calculation describing the

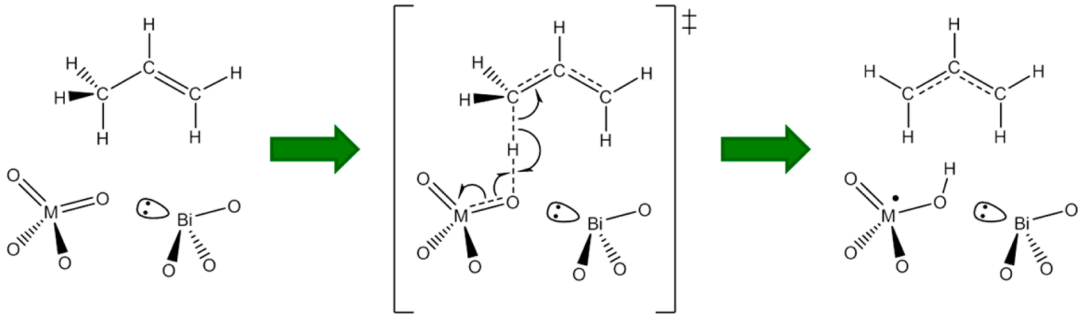

Figure 6. Generic mechanism for propene activation involving a catalyst M═O bond.

dx.doi.org/10.1021/ja5051555 | J. Am. Chem. Soc. 2014, 136, 13684−13697

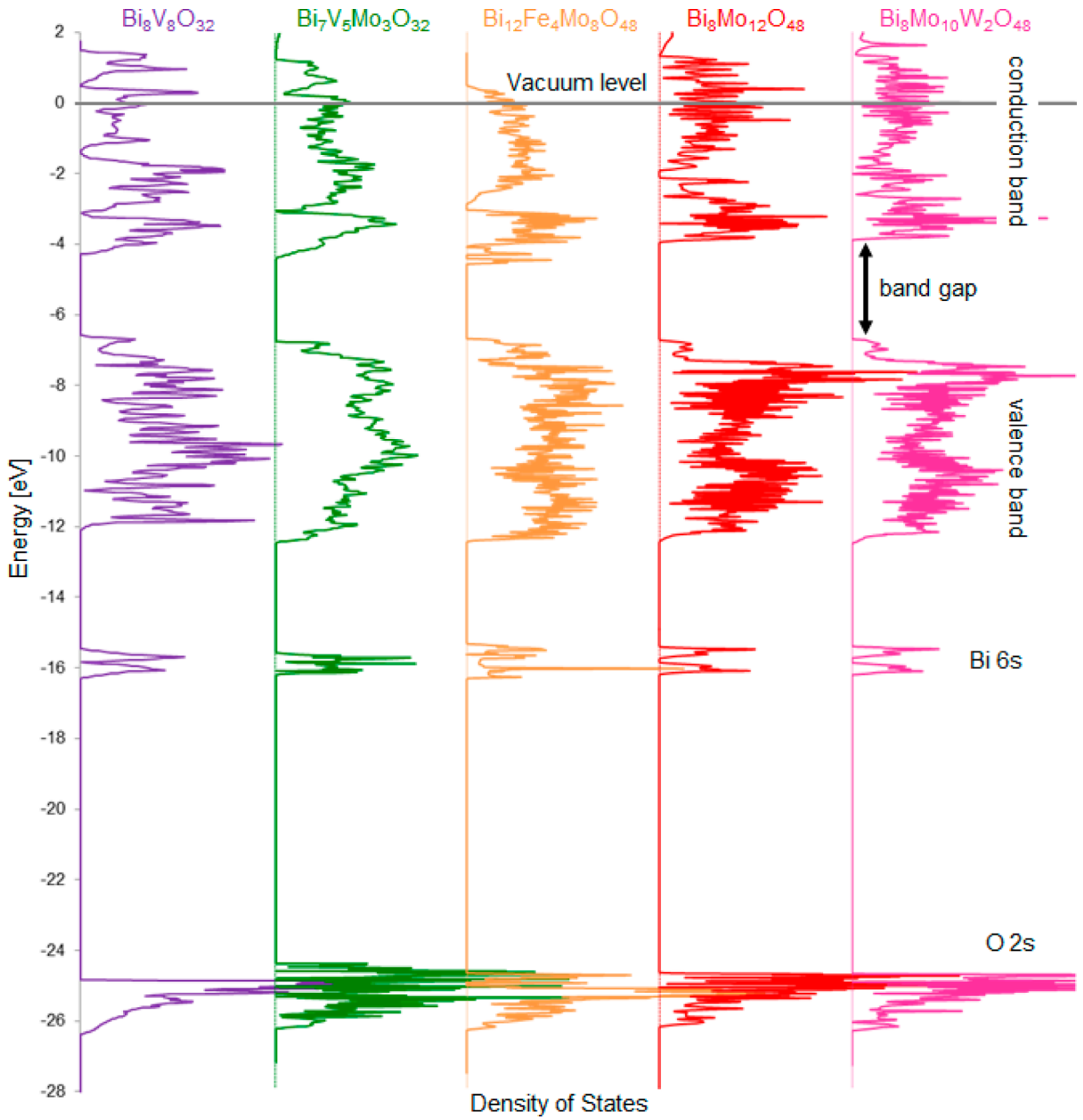

Figure 8. From left to right: calculated density of states for $BiVO_4$ (purple), $Bi_7V_5Mo_3O_{32}$ (green), $Bi_3FeMo_2O_{12}$ (orange), $Bi_2Mo_3O_{12}$ (red), and $Bi_2Mo_{2.5}W_{0.5}O_{12}$ (pink).

states involved in a UV−visible absorption experiment—reflects the commonality of the physics of these two processes.

The difference between E_{hyb} values for $BiVO_4$ and $Bi_2Mo_3O_{12}$ amounts to ∼9 kcal/mol, consistent with the ∼5 kcal/mol difference in observed activation energies for propene oxidation over these two catalysts. Even better agreement between theory and experiment could be obtained by including spin−orbit coupling effects in the calculation: previous analysis[73,74] found that spin−orbit coupling effects reduce the barrier to C−H activation on $Bi_2Mo_3O_{12}$ by 4.6 kcal/mol, whereas a much smaller 0.5 kcal/mol reduction in barrier occurs for $BiVO_4$ due to weaker spin−orbit coupling for V 3d vs Mo 4d orbitals. However, incorporation of spin−orbit coupling effects requires detailed knowledge of the potential energy surface near the transition state for C−H bond activation, where these effects are manifest. By contrast, no transition state calculations are required to obtain the terms used in the Born−Haber cycle presented above. Rather, knowledge of the initial state and final state for C−H bond activation and consideration of the bond-breaking and bond-forming processes linking these states are sufficient not only to explain differences in catalytic performance between $BiVO_4$ and $Bi_2Mo_3O_{12}$ but, further, to link these differences to a simple experimental observable: the band-gap energy.

In order to complete the discussion of the relationship of catalyst band gaps to apparent activation energies, the change in enthalpy upon adsorption needs to be considered. Under the reaction conditions used in this work to extract apparent activation energies, the resting state of the catalyst is the bare, fully oxidized oxide surface. The oxidation of propene is initiated by reversible physisorption of propene gas to the active site, followed by rate-limiting activation of an allylic C−H bond. The apparent activation energy assessed by experiment comprises the sum of the energies of both of these steps,

dx.doi.org/10.1021/ja5051555 | J. Am. Chem. Soc. 2014, 136, 13684−13697

whereas the intrinsic activation energy estimated from Born−Haber cycle analysis addresses only the C−H bond activation step. An estimate for the apparent activation energy can therefore be obtained by adding the adsorption enthalpy to the calculated intrinsic activation energy. The change in enthalpy upon adsorption of propene on bismuth molybdate has been measured experimentally at −7 to −8 kcal/mol.[97,98] Unfortunately, the enthalpies of adsorption of propene on bismuth vanadate or on V-, Fe-, or W-substituted bismuth molybdates have not been reported in the literature to the best of our knowledge. However, given the purely van der Waals nature of the interaction between propene and support, and the structural similarity among the oxide phases under consideration, it is reasonable to expect the adsorption enthalpy to be relatively insensitive to composition. Support for this expectation is provided by DFT calculations, which yield adsorption enthalpies of −8.2 kcal/mol on $BiVO_4$, −7.8 kcal/mol on $Bi_7V_5Mo_3O_{32}$, and −6.4 kcal/mol on $Bi_2Mo_3O_{12}$ (taking adsorption enthalpy as the enthalpy of the adsorbed state minus the separate enthalpies of the model catalyst surface and propene). Calculated heats of adsorption are used with caution, as the M06-L functional employed here does not contain an explicit van der Waals interaction term. It is, however, parametrized using training sets including systems dominated by dispersive interactions and has proven successful in capturing such interactions in a number of other systems.[74,99−102] It is therefore expected that the calculated heats of adsorption presented here are of sufficient accuracy to provide useful estimates of propene adsorption enthalpies on the oxide phases examined. The estimated ∼2 kcal/mol variation in heat of adsorption with composition is comparable in magnitude to the ∼2 kcal/mol variations with composition in $E_{stretch}$ and E_{OH} in the Born−Haber cycle and remains significantly smaller in magnitude than the variation in E_{hyb}. Thus, even after accounting for adsorption enthalpy, the observed trends in apparent activation energy with composition are primarily attributable to changes in band-gap energy.

Taking the change in enthalpy for propene adsorption on $BiVO_4$ to be −8 kcal/mol and adding it to the values of E_{C-H} (88.2 kcal/mol), $E_{stretch}$ (20.9 kcal/mol), E_{hyb} (30.1 kcal/mol), and E_{OH} (−115.8 kcal/mol) yields an estimated apparent activation barrier of 15.4 kcal/mol, in excellent agreement with the experimentally observed apparent activation energy of 14.5 kcal/mol. Likewise, taking the change in enthalpy for propene adsorption on $Bi_2Mo_3O_{12}$ to be −7 kcal/mol and adding it to the values of E_{C-H} (88.2 kcal/mol), $E_{stretch}$ (23.0 kcal/mol), E_{hyb} (39.0 kcal/mol), and E_{OH} (−117.9 kcal/mol) yields an estimated apparent activation barrier of 25.3 kcal/mol, which can be compared to the 19.9 kcal/mol measured experimentally. As noted above, inclusion of spin−orbit coupling effects would provide even closer agreement between estimate and experiment (i.e., estimated barriers of 14.9 kcal/mol for $BiVO_4$ and 20.7 kcal/mol for $Bi_2Mo_3O_{12}$). The close agreement between estimated and measured apparent activation barriers confirms that all of the physical processes contributing to the observed activation barrier have been accounted for in the Born−Haber analysis. This analysis, in turn, provides a rationale for the observed lower barrier to propene activation over $BiVO_4$ as compared to $Bi_2Mo_3O_{12}$.

Density of States Calculations. To understand why the band-gap energy is a good descriptor of catalytic activity for mixed phases containing both Mo and V, Fe, or W, it is necessary to examine more closely how the electronic states involved in LMCT excitation are affected by composition. For all materials examined, the highest occupied crystal orbital involves the nonbonding O 2p states, which have t_1 symmetry with respect to the tetrahedral oxoanions. The character of the lowest unoccupied, metal-centered electronic states involved in the LMCT excitation, however, depends on the metal(s) present in the catalyst. To obtain a more complete understanding of the electronic structure of substituted bismuth molybdate-based catalysts, density functional theory calculations were carried out on five representative compositions. Crystal structures taken from the literature were used to generate models for $BiVO_4$, $Bi_2Mo_3O_{12}$, and $Bi_3FeMo_2O_{12}$. A single material of composition $Bi_7V_5Mo_3O_{32}$ ($x = 0.375$) was used to explore electronic effects in $Bi_{1-x/3}V_{1-x}Mo_xO_4$, and a single material of composition $Bi_8Mo_{10}W_2O_{48}$ was used to explore electronic effects in $Bi_2Mo_{3-y}W_yO_{12}$. We note that prior studies of the electronic structure of $BiVO_4$ have shown good agreement between theory and experiment.[103−108] To our knowledge, the present study represents the first investigation of the electronic structure of $Bi_2Mo_3O_{12}$, $Bi_3FeMo_2O_{12}$, $Bi_{1-x/3}V_{1-x}Mo_xO_4$, or $Bi_2Mo_{3-y}W_yO_{12}$ using density functional theory.

The density of states for $BiVO_4$, $Bi_7V_5Mo_3O_{32}$, $Bi_3FeMo_2O_{12}$, $Bi_2Mo_3O_{12}$, and $Bi_2Mo_{2.5}W_{0.5}O_{12}$ are presented in Figure 8. The bands centered at −25.3 and −15.9 eV correspond to O 2s and Bi 6s electrons, respectively. (Bi 5d core states, not explicitly modeled in these calculations, would appear below −28 eV; they have been shown to play no role in bonding in bismuth oxides[109]). Although O 2s and Bi 6s orbitals are treated as valence orbitals in the calculations, the narrow width of these bands and the lack of mixing with other orbitals suggest that these states are essentially corelike and ionic in character. The corelike character of these states is further underscored by the finding that their energies do not vary with composition: the density-weighted average energy of the O 2s states is within 0.10 eV of −25.30 eV, and the density-weighted average energy of the Bi 6s states is within 0.05 eV of −15.90 eV, in all compositions studied. For comparison, the energy of the O 2s orbital on an isolated O atom is calculated to be −25.2 eV.

The valence states run from near −13 to −7 eV, while the conduction band states begin near −4.5 eV and run past the vacuum level. $Bi_3FeMo_2O_{12}$ also contains two midgap states just below the conduction band; the significance of these states is discussed more fully below. The band gap is calculated as the difference in energy between the lowest energy conduction band state and the highest energy valence band state. As compiled in Table 1, the density of states calculations yielded band gaps in excellent agreement with those measured experimentally.

To determine the effect of V substitution on the electronic structure of $Bi_2Mo_3O_{12}$, the atom-projected density of states has been evaluated for $Bi_7V_5Mo_3O_{32}$. As shown in Figure 9, the valence states of $Bi_7V_5Mo_3O_{32}$ run from −12.5 to −6.8 eV, while the conduction band states begin near −4.5 eV and run up to the vacuum level. (Recall that the energy abscissa in Figure 9 has been referenced to the vacuum state energy.) The valence states can loosely be grouped into four regions. The region from −12.5 to −11 eV is comprised primarily of Mo−O σ and π bonding states built from Mo 4d and O 2p orbitals. This region also contains a smaller contribution from Bi 6p orbitals, which mix with O 2p orbitals to produce Bi−O σ bonds. The region from −11 to −9 eV is dominated by V−O σ and π bonds built from V 3d and O 2p orbitals. The region

dx.doi.org/10.1021/ja5051555 | J. Am. Chem. Soc. 2014, 136, 13684−13697

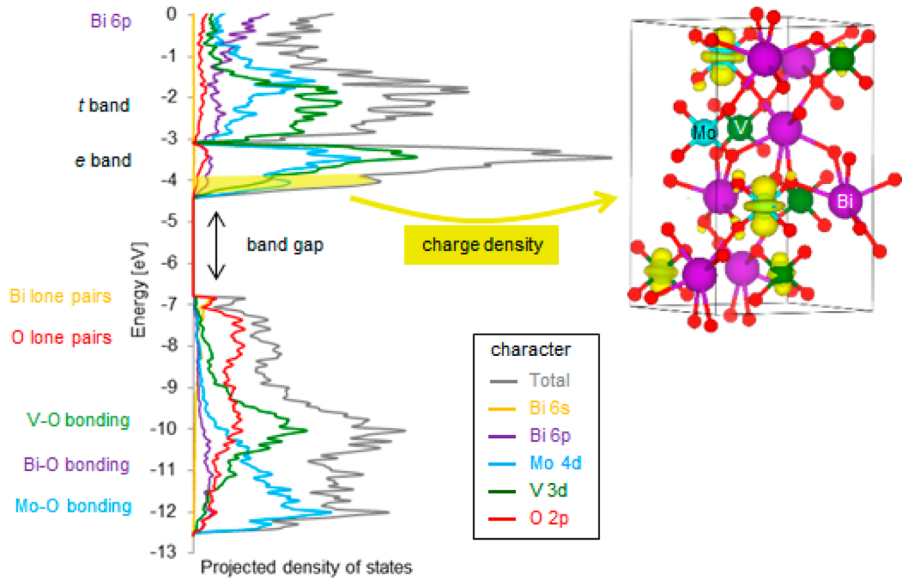

Figure 9. Atom-projected density of states for $Bi_7V_5Mo_3O_{32}$. A map of the charge density of the states from −4.5 to −4.0 eV is shown on the right.

from −9 to −7 eV has primarily O 2p character and is attributed to lone-pair-like states on oxygen. The narrow region from −7.1 eV to the valence band edge at −6.8 eV remains predominantly O 2p in character, but also contains an important contribution from Bi 6s states. These states have Bi−O σ^* character and are responsible for the existence of the "stereochemically active lone pair" on bismuth.[110,111] We have shown elsewhere that these lone pairs play an instrumental role in creating catalytically active sites on the surface of the $Bi_2Mo_3O_{12}$ catalyst.[73,74]

The conduction band states can also be categorized according to the dominant character of the states in each energy region. The V 3d and Mo 4d states on tetrahedrally coordinated vanadate and molybdate ions are split by the local crystal field into lower energy e states (d_{z^2} and $d_{x^2-y^2}$ orbitals) and higher energy t_2 states (d_{xy}, d_{yz}, and d_{xz} orbitals). In $Bi_7V_5Mo_3O_{32}$, the e states run from the conduction band edge at −4.48 eV to −3.08 eV, while the t_2 states begin at −3.08 eV and run up to roughly −1.2 eV. The states above this energy are primarily derived from the empty Bi 6p orbitals, which also contribute slightly to the e and t_2 bands. Though none of the conduction band states have strong O 2p character, all of them have Mo−O, V−O, or Bi−O antibonding character.

In scheelite-structured materials, MO_4^{n-} ions are not perfectly tetrahedral, experiencing a small oblate tetragonal distortion. As a result, the d_{z^2} orbitals are lowered in energy relative to the $d_{x^2-y^2}$ orbitals. Although the distortion is not large enough to split the e band in $Bi_7V_5Mo_3O_{32}$ into separate d_{z^2} and $d_{x^2-y^2}$ bands, the state right at the conduction band edge has almost purely d_{z^2} character. A map of the charge density distribution for this state is shown at the right in Figure 9. In accordance with the presence of both V 3d and Mo 4d states at the bottom of the e band, significant charge density is present in d_{z^2} orbitals on both V and Mo centers. (The greater spatial extension of the larger Mo 4d orbitals compared to the smaller V 3d orbitals is also visible.) The mixing of V 3d and Mo 4d states in the e band and the contribution of both V and Mo centers to the charge density shown in Figure 9 provide an explanation for the results seen in Figure 1: both V 3d and Mo 4d orbitals contribute to the character of the states into which electrons are excited during the band-gap measurement. Increasing vanadium content in $Bi_{1-x/3}V_{1-x}Mo_xO_4$ increases the contribution from lower energy V 3d states to the e band, lowering the LMCT excitation energy. It is for this reason that only a single adsorption edge at a composition-dependent energy is observed in $Bi_{1-x/3}V_{1-x}Mo_xO_4$ solid solutions.

The effect of W substitution in $Bi_2Mo_{3-y}W_yO_{12}$ materials can be understood using the same analysis. The e-band states at the bottom of the conduction band are comprised of both Mo 4d and W 5d orbitals, with the energy of the e band (and therefore the LMCT excitation energy) dependent upon the relative proportions of Mo and W present. In contrast to the case of vanadium substitution, however, tungsten substitution increases the LMCT excitation energy. This can be understood by examining the data in Table 4. The average energy of the V 3d orbitals is lower than the average energy of the Mo 4d orbitals, so V substitution tends to lower the e-band energy. (Again, these energies are referenced to the vacuum state.) Conversely, the average energy of the W 5d orbitals is higher than that of the Mo 4d orbitals, so W substitution leads to an increase of the e-band energy. In both cases, efficient mixing among d orbitals leads to a single, mixed-character e band and a single, composition-dependent LMCT absorption edge energy.

Table 4. Calulcated Average d Orbital Energies (eV)

orbital	Fe 3d	V 3d	Mo 4d	W 5d
energy	−6.66	−5.02	−4.48	−4.02

The results in Table 4 indicate that since the 3d orbitals in Fe are even lower in energy than the 3d orbitals in V, substitution of Fe into bismuth molybdate should have an even greater energy-lowering effect on the LMCT excitation energy than substitution with V. As shown in Figure 2, Fe substitution does indeed lower the LMCT excitation energy. However, a comparison between $Bi_3FeMo_2O_{12}$ and $Bi_{2.4}V_{1.2}Mo_{1.8}O_{12}$ (x = 0.60) reveals that the band gap in the Fe-substituted material is actually slightly larger than in a V-substituted material with a similar degree of substitution. The comparatively lower effectiveness of the Fe 3d orbitals in lowering the e-band energy in $Bi_3FeMo_2O_{12}$ vs that of the V 3d orbitals in

dx.doi.org/10.1021/ja5051555 | J. Am. Chem. Soc. 2014, 136, 13684−13697

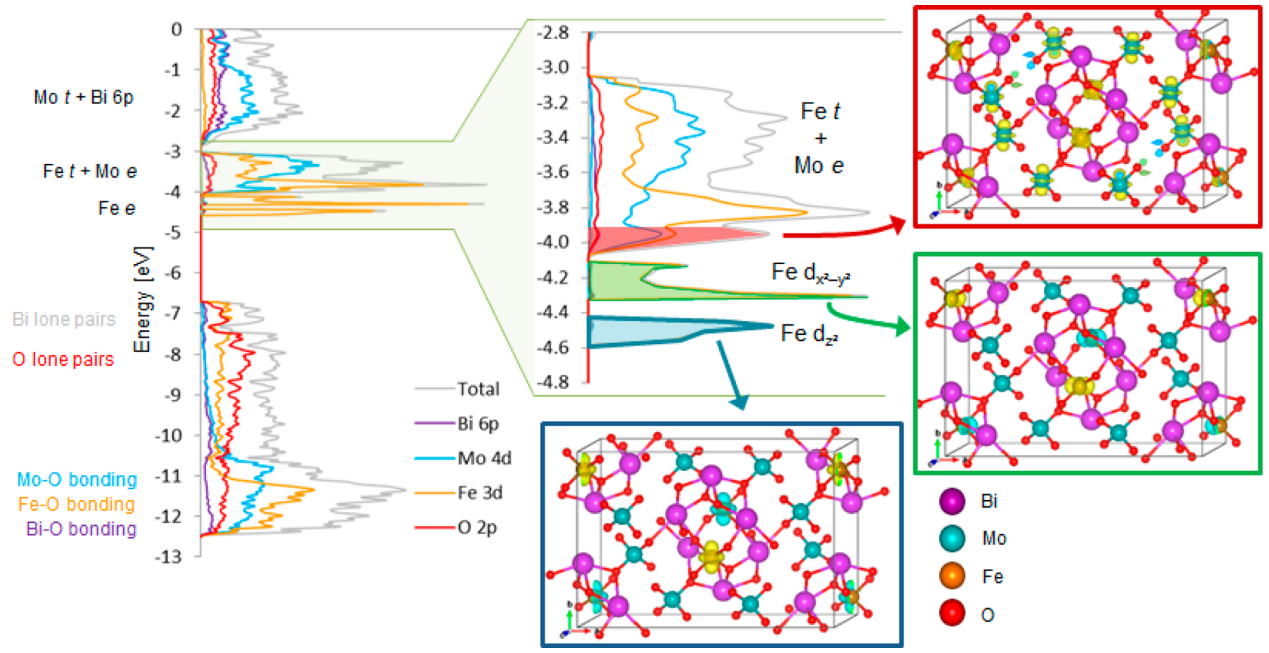

Figure 10. Site-projected density of states for $Bi_3FeMo_2O_{12}$. The conduction band states between −2.8 and −4.8 eV are shown in greater detail in the center, with charge density maps provided for the midgap Fe d_{z^2} and $Fe_{x^2-y^2}$ states and first conduction band state.

Table 5. Calculated Values of Band-Gap Energies and Energies of e-Band Bottom, Center, Top, and Width (eV)

	$BiVO_4$	$Bi_7V_5Mo_3O_{32}$	$Bi_3FeMo_2O_{12}$	$Bi_2Mo_3O_{12}$	$Bi_2Mo_{2.5}W_{0.5}O_{12}$
band gap	2.28	2.38	2.64	2.80	2.84
e-band bottom	−4.29	−4.42	−4.09	−3.95	−3.88
e-band center	−3.64	−3.60	−3.54	−3.30	−3.26
e-band top	−3.11	−3.08	−3.07	−2.65	−2.60
e-band width	1.18	1.34	1.02	1.30	1.28

$Bi_{1-x/3}V_{1-x}Mo_xO_4$ can be understood by examining the projected density of states for $Bi_3FeMo_2O_{12}$ presented in Figure 10. In $Bi_{1-x/3}V_{1-x}Mo_xO_4$, the states at the bottom of the conduction band arise from the overlap between Mo 4d states of e symmetry and lower energy V 3d states of e symmetry. (The Mo 4d and V 3d states of t_2 symmetry also overlap to create a higher energy t_2 band, which lies above −3.1 eV in Figure 9.) By contrast, in $Bi_3FeMo_2O_{12}$, the e symmetry Fe 3d states are too low in energy to overlap effectively with Mo 4d states. Instead, the Fe 3d e states form a pair of narrow, localized bands that lie below the conduction band edge energy. (These states are in fact so localized that the slight oblate tetragonal distortion of the nominally tetrahedral oxoanions in the scheelite crystal structure completely resolves the nominally e symmetry Fe 3d states into separate d_{z^2} and $d_{x^2-y^2}$ bands.) These are best considered midgap states; excitation of occupied Fe 3d electrons into these states gives rise to the pre-edge absorption shown in Figure 2. The lowering of the conduction band edge energy in $Bi_3FeMo_2O_{12}$ relative to that in $Bi_2Mo_3O_{12}$ instead arises from mixing between Mo 4d states of e symmetry and Fe 3d states of t_2 symmetry. This mixing gives rise to the charge density shown in the upper right inset in Figure 10. While Fe 3d states of t_2 symmetry are still lower in energy than Mo 4d states of e symmetry, they are not as low in energy as Fe 3d states of e symmetry. It is for this reason that substitution with Fe lowers the LMCT excitation energy, but not as effectively as might have been expected from the results in Table 4.

The contrast between the mixing of Mo 4d states with V 3d states vs with Fe 3d states illustrates that a metric attempting to predict the effect of cation substitution on the LMCT excitation energy that is based only on the average energy of the d states of the substituting atom (see Table 4) would be not be appropriate. Greater insight into the ability of a substituent cation to influence the LMCT excitation energy can be obtained by considering not only the average energies of the d states, but also their bandwidths. As shown in Table 5, the widths of the e-band states in $BiVO_4$ and $Bi_2Mo_3O_{12}$ are 1.18 and 1.30 eV, respectively. The somewhat greater width of the e band in $Bi_2Mo_3O_{12}$ compared to $BiVO_4$ is a consequence of greater spatial overlap between the larger Mo 4d orbitals compared to the smaller V 3d orbitals (as seen in the inset in Figure 9). According to Table 4, the average V 3d and Mo 4d orbital energies differ by only ∼0.5 eV, which is less than the width of the e bands arising from V 3d and Mo 4d orbitals. The result is the effective overlap between V 3d and Mo 4d states in $Bi_{1-x/3}V_{1-x}Mo_xO_4$ solid solutions. The difference in average orbital energies between the Fe 3d and Mo 4d orbitals, however, is greater than 2 eV. In addition, the greater effective nuclear charge on Fe vs V renders the Fe 3d orbitals even more compact than the V 3d orbitals, resulting in poorer through-space overlap and reduced bandwidth: even including the gap between the Fe $3d_{z^2}$ and Fe $3d_{x^2-y^2}$ states, the Fe e-band width in $Bi_3FeMo_2O_{12}$ is only 0.46 eV. The widths of the Fe 3d and Mo 4d e bands are not great enough to span the >2 eV

dx.doi.org/10.1021/ja5051555 | J. Am. Chem. Soc. 2014, 136, 13684−13697

difference in the energies between these orbitals, and as a result, the Fe 3d and Mo 4d e states do not mix.

Although not explored further in the present study, the orbital mixing effects observed here are likely to be general features in single-phase metal oxides containing multiple transition-metal species. With knowledge of the center and bandwidth of the e band in tetrahedral systems or the t_{2g} band in octahedral systems, it should be possible to systematically tune the LMCT excitation energy. For catalytic systems in which the activation of substrate bonds involves LMCT-like excited states, systematic tuning of the LMCT excitation energy should in turn provide a means for altering catalytic activity. Although only scheelite-structured materials have been examined here, these effects should be generally observable in other mixed metal oxide systems, including those based on zircons,[112] perovskites,[36,37,113,114] spinels,[115,116] rutile,[117] and other structures.[118] More work in this area is clearly required.

CONCLUSIONS

A model has been proposed to explain the observed correlation of the activation barrier propene oxidation to acrolein over a mixed metal oxide with the ligand-to-metal charge transfer (LMCT) excitation energy of the oxide. This excitation energy corresponds to the band-gap energy for metal oxides containing transition metals in their highest oxidations states. We note that this model should also apply to any oxidation reaction in which activation of the reactive substrate occurs through a transition state involving rehybridization of a catalyst M=O bond in the rate-controlling catalytic step. We have shown that the model successfully explains the variations in the apparent activation energy observed for the oxidation of propene to acrolein over catalysts based on bismuth molybdate and containing varying proportions of vanadium, tungsten, or iron. Substitution of vanadium or iron for molybdenum reduces the apparent activation energy by lowering the LMCT energy. In bismuth molybdates, the LMCT excitation occurs between oxygen lone pair states at the top of the valence band and e symmetry Mo 4d states at the bottom of the conduction band. Substitution by vanadium lowers the LMCT excitation energy by mixing the e symmetry Mo 4d states with lower energy e symmetry V 3d states. Substitution by iron also lowers the LMCT excitation energy. However, in this case the e symmetry Mo 4d states mix instead with t_2 symmetry Fe 3d states; the e symmetry Fe 3d states are too low in energy to mix effectively and instead form a pair of midgap states. Substitution by tungsten increases the LMCT excitation energy, as e symmetry Mo 4d states mix with higher energy e symmetry W 5d states. In each case, the LMCT excitation energy can be rationalized by considering both the average energy and the bandwidth of the metal d-orbital states. With knowledge of these orbital properties, it becomes possible to systematically tune the LMCT excitation energy in mixed metal oxides. Such tuning allows the rational formulation of more active mixed metal oxide oxidation catalysts in at least one family of materials, and it is believed that other systems are likely to exhibit similar effects.

ASSOCIATED CONTENT

Supporting Information

Additional details on experimental and theoretical methods; additional experimental results, including X-ray diffraction patterns, Raman and diffuse reflectance UV−visible spectra, and plots of catalyst selectivity vs conversion; and additional theoretical results, including investigation of a possible mechanism for propene C−H bond activation by bismuth vanadate and structures and energies of models used in density functional theory calculations. These materials are available free of charge via the Internet at http://pubs.acs.org.

AUTHOR INFORMATION

Corresponding Author

bell@uclink.berkeley.edu

Author Contributions

†These authors contributed equally to this work.

Notes

The authors declare no competing financial interest.

ACKNOWLEDGMENTS

This work was funded by Director, Office of Science, Office of Basic Energy Sciences of the U.S. Department of Energy under Contract No. DE-AC03-76SF00098. Portions of this research were carried out at the Argonne National Laboratory (ANL), managed by the University of Chicago-Argonne, LLC, for the U.S. Department of Energy's Office of Science. XANES experiments were conducted at the Advanced Photon Source at Argonne National Laboratory, supported by the U.S. Department of Energy, Office of Science, under contract DE-AC02-06CH11357. DFT calculations were conducted on the Hopper workstation at the National Energy Research Scientific Computing Center, which is supported by the U.S. Department of Energy, Office of Basic Science, under contract DE-AC02-50CH11231. Additional calculations were performed at the University of California—Berkeley Molecular Graphics and Computation Facility, which is supported by NSF Grant CHE-0840505. The authors would also like to acknowledge Dr. John Katsoudas and Dr. Jeffrey T. Miller, for assistance in conducting XANES experiments, and Anton Mlinar and Rachel Licht, for useful discussions.

REFERENCES

(1) Hammer, B.; Nørskov, J. K. *Adv. Catal.* **2000**, *45*, 71.
(2) Ruban, A.; Hammer, B.; Stoltze, P.; Skriver, H. L.; Nørskov, J. K. *J. Mol. Catal.* **1999**, *115*, 421.
(3) Lu, C.; Lee, I. C.; Masel, R. I.; Wieckowski, A.; Rice, C. *J. Phys. Chem. A* **2002**, *106*, 3084.
(4) Kitchin, J. R.; Nørskov, J. K.; Barteau, M. A.; Chen, J. G. *J. Chem. Phys.* **2004**, *120*, 10240.
(5) Stamenkovic, V.; Mun, B. S.; Mayrhofer, K. J. J.; Ross, P. N.; Markovic, N. M.; Rossmeisl, J.; Greeley, J.; Nørskov, J. K. *Angew. Chem.* **2006**, *118*, 2963.
(6) Xin, H.; Linic, S. *J. Chem. Phys.* **2010**, *132*, 221101.
(7) Greeley, J.; Stephens, I. E. L.; Bondarenko, A. S.; Johansson, T. P.; Hansen, H. A.; Jaramillo, T. F.; Rossmeisl, J.; Chorkendorff, I.; Nørskov, J. K. *Nat. Chem.* **2009**, *1*, 552.
(8) Greeley, J.; Mavrikakis, M. *Nat. Mater.* **2004**, *3*, 810.
(9) Huo, C.-F.; Li, Y.-W.; Wang, J.; Jiao, H. *J. Am. Chem. Soc.* **2009**, *131*, 14713.
(10) Albonetti, S.; Cavani, F.; Trifirò, F. *Catal. Rev.-Sci. Eng.* **1996**, *38*, 413.
(11) Albonetti, S.; Cavani, F.; Trifirò, F.; Venturoli, P.; Calestani, G.; López Granados, M.; Fierro, J. L. G. *J. Catal.* **1996**, *160*, 52.
(12) Bañares, M. A. *Catal. Today* **1999**, *51*, 319.
(13) Hodnett, B. K. *Cat Rev.: Sci. Technol.* **1985**, *27*, 373.
(14) Grasselli, R. K. *Top. Catal.* **2001**, *14*, 93.
(15) Vining, W. C.; Goodrow, A.; Strunk, J.; Bell, A. T. *J. Catal.* **2010**, *270*, 163.
(16) Zhang, W.; Desikan, A.; Oyama, S. T. *J. Phys. Chem.* **1995**, *99*, 11468.

(17) Nikolov, V.; Klissurski, D.; Anastasov, A. *Cat Rev.: Sci. Eng.* **1991**, *33*, 319.
(18) Liu, Z.; Peng, F.; Liu, X. *Adv. Mater. Res.* **2012**, *119*, 550.
(19) Heck, R. M. *Catal. Today* **1999**, *53*, 519.
(20) Kang, M.; Park, E. D.; Kim, J. M.; Yie, J. E. *Appl. Catal., A* **2007**, *327*, 261.
(21) Li, K.-T.; Huang, M.-Y.; Cheng, W.-D. *Ind. Eng. Chem. Res.* **1996**, *35*, 621.
(22) Peacock, J. M.; Parker, A. J.; Ashmore, P. G.; Hockey, J. A. *J. Catal.* **1969**, *15*, 398.
(23) Keulks, G. W.; Yu, Z.; Krenzke, L. D. *J. Catal.* **1983**, *84*, 38.
(24) Baca, M.; Pigamo, A.; Dubois, J. L.; Millet, J. M. M. *Top. Catal.* **2003**, *23*, 39.
(25) Bielański, A.; Najbar, M. *Appl. Catal., A* **1997**, *157*, 223.
(26) Burriesci, N.; Garbassi, F.; Petrera, M.; Petrini, G. *J. Chem. Soc., Faraday Trans 1* **1982**, *78*, 817.
(27) Vieira Soares, A. P.; Farinha Portela, M.; Kiennemann, A. *Catal. Rev.; Sci. Eng.* **2005**, *47*, 125.
(28) López Nieto, J. M. *Top. Catal.* **2006**, *41*, 3.
(29) Wachs, I. E.; Routray, K. *ACS Catal.* **2012**, *2*, 1235.
(30) Campbell, C. T.; Sauer, J. *Chem. Rev.* **2013**, *113*, 3859.
(31) Campbell, C. T.; Sellers, J. R. V. *Chem. Rev.* **2013**, *113*, 4106.
(32) Burcham, L. J.; Briand, L. E.; Wachs, I. E. *Langmuir* **2001**, *17*, 6164.
(33) Goodrow, A.; Bell, A. T. *J. Phys. Chem. C* **2008**, *112*, 13204.
(34) Sleight, A. W.; Linn, W. J. *Ann. N. Y. Acad. Sci.* **2006**, 22.
(35) McFarland, E. W.; Metiu, H. *Chem. Rev.* **2013**, *113*, 4391.
(36) Calle-Vallejo, F.; Inoglu, N. G.; Su, H.-Y.; Martínez, J. I.; Man, I. C.; Koper, M. T. M.; Kitchin, J. R.; Rossmeisl, J. *Chem. Sci.* **2013**, *4*, 1245.
(37) Lee, Y.-L.; Kleis, J.; Rossmeisl, J.; Shao-Horn, Y.; Morgan, D. *Energy Environ. Sci.* **2011**, *4*, 3966.
(38) Moriceau, P.; Lebouteiller, A.; Bordes, E.; Courtine, P. *Phys. Chem. Chem. Phys.* **1991**, *1*, 5735.
(39) Moriceau, P.; Tauok, B.; Bordes, E.; Courtine, P. *Catal. Today* **2000**, *61*, 197.
(40) Bordes-Richard, E. *Top. Catal.* **2008**, *50*, 82.
(41) Duffy, J. A.; Ingram, M. D. *J. Am. Chem. Soc.* **1971**, *24*, 6448.
(42) Dimitrov, V.; Sakka, S. *J. Appl. Phys.* **1996**, *79*, 1736.
(43) Lebouteiller, A.; Courtine, P. *J. Solid State Chem.* **1998**, *137*, 94.
(44) Duffy, J. A.; Ingram, M. D. *J. Inorg. Nucl. Chem.* **1976**, *38*, 1831.
(45) Pecoraro, T. A.; Chiannelli, R. R. *J. Catal.* **1981**, *67*, 430.
(46) Toulhoat, H.; Raybaud, P.; Kasztelan, S.; Kresse, G.; Hafner, J. *Catal. Today* **1999**, *50*, 629.
(47) Chianelli, R. R.; Berhault, G.; Raybaud, P.; Kasztelan, S.; Hafner, J.; Toulhoat, H. *Appl. Catal., A* **2002**, *227*, 83.
(48) Toulhoat, H.; Raybaud, P. *J. Catal.* **2003**, *216*, 63.
(49) Guernalec, N.; Geantet, C.; Cseri, T.; Vrinat, M.; Toulhoat, H.; Raybaud, P. *Dalton Trans.* **2010**, *39*, 8420.
(50) Routray, K.; Briand, L. E.; Wachs, I. E. *J. Catal.* **2008**, *256*, 145.
(51) Idriss, H.; Seebauer, E. G. *Catal. Lett.* **2000**, *66*, 139.
(52) Rideout, V. L. *Solid-State Electron.* **1975**, *18*, 541.
(53) Nozik, A. J.; Memming, R. *J. Phys. Chem.* **1996**, *100*, 13061.
(54) Chen, X.; Shen, S.; Guo, L.; Mao, S. S. *Chem. Rev.* **2010**, *110*, 6503.
(55) Xu, Y.; Schoonen, M. A. A. *Am. Minerol.* **2000**, *85*, 543.
(56) Fukui, K.; Teijiro, Y.; Haruo, S. *J. Chem. Phys.* **1952**, *20*, 722.
(57) Anslyn, E. V.; Dougherty, D. A. *Modern Physical Organic Chemistry*; University Science Books: Herndon, VA, 2006.
(58) Raybaud, P.; Hafner, J.; Kresse, G.; Toulhoat, H. *J. Phys.: Condens. Matter* **1997**, *9*, 11107.
(59) Adams, C. R.; Jennings, T. J. *J. Catal.* **1963**, *2*, 63.
(60) Adams, C. R.; Jennings, T. J. *J. Catal.* **1964**, *3*, 549.
(61) McCain, C. C.; Gough, G.; Godin, G. W. *Nature* **1963**, *198*, 989.
(62) Ueda, W.; Asakawa, K.; Chen, C.-L.; Moro-Oka, Y.; Ikawa, T. *J. Catal.* **1986**, *101*, 360.
(63) Krenzke, L. D.; Keulks, G. W. *J. Catal.* **1980**, *61*, 316.
(64) Keulks, G. W. *J. Catal.* **1970**, *19*, 232.
(65) Burrington, J. D.; Kartisek, C. T.; Grasselli, R. K. *J. Catal.* **1980**, *63*, 235.
(66) Mars, P.; van Krevelen, D. W. *Chem. Eng. Sci.* **1954**, *3*, 41.
(67) Zhai, Z.; Getsoian, A.; Bell, A. T. *J. Catal.* **2013**, *308*, 25.
(68) Wong, H.-W.; Cesa, M. C.; Golab, J. T.; Brazdil, J. F.; Green, W. H. *Appl. Catal. A* **2006**, *303*, 177.
(69) Jang, Y.; Goddard, W. A. *Top. Catal.* **2001**, *15*, 273.
(70) Jang, Y.; Goddard, W. A. *J. Phys. Chem. B* **2002**, *106*, 5997.
(71) Pudar, S.; Oxgaard, J.; Chenoweth, K.; van Duin, A. C. T.; Goddard, W. A. *J. Phys. Chem. C* **2007**, *111*, 16045.
(72) Goddard, W. A.; van Duin, A.; Chenoweth, K.; Cheng, M. J.; Pudar, S.; Oxgaard, J.; Merinov, B.; Jang, Y. H.; Persson, P. *Top. Catal.* **2006**, *38*, 93.
(73) Getsoian, A.; Shapovalov, V.; Bell, A. T. *J. Phys. Chem. C* **2013**, *117* (14), 7123.
(74) Getsoian, A.; Bell, A. T. *J. Phys. Chem. C* **2013**, *117* (48), 25562.
(75) Kresse, G.; Furthmüller, J. *Comput. Mater. Sci.* **1996**, *6*, 15.
(76) Blochl, P. E. *Phys. Rev. B* **1994**, *50*, 17953.
(77) Kresse, G.; Joubert, D. *Phys. Rev. B* **1999**, *59*, 1758.
(78) Kresse, G.; Furthmüller, J. *Phys. Rev. B* **1996**, *54*, 11169.
(79) Zhao, Y.; Truhlar, D. G. *J. Chem. Phys.* **2006**, *125*, 194101.
(80) Zhao, Y.; Truhlar, D. G. *Theor. Chem. Acc.* **2008**, *120*, 215.
(81) Sleight, A. W.; Chen, H.-Y.; Ferretti, A.; Cox, D. E. *Mater. Res. Bull.* **1979**, *14*, 1571.
(82) Theobald, F.; Laarif, A.; Hewat, A. W. *Mater. Res. Bull.* **1985**, *20*, 653.
(83) Jeitschko, W.; Sleight, A. W.; McClellan, W. R.; Weiher, J. F. *Acta Crystallogr.* **1976**, *B32*, 1163.
(84) Koopmans, T. *Physica (Elsevier)* **1934**, *1*, 104.
(85) Tokunaga, S.; Kato, H.; Kudo, A. *Chem. Mater.* **2001**, *13*, 4624.
(86) de la Cruz, A. M.; Alfaro, S. O. *Solid State Sci.* **2009**, *11*, 829.
(87) Fan, H. Y. *Phys. Rev.* **1951**, *82*, 900.
(88) Varshni, Y. P. *Physica* **1967**, *34*, 149.
(89) Ayame, A.; Uchida, K.; Iwataya, M.; Miyamoto, M. *Appl. Catal. A* **2002**, *227*, 7.
(90) Peacock, J. M.; Sharp, M. J.; Parker, A. J.; Ashmore, P. G.; Hockey, J. A. *J. Catal.* **1969**, *15*, 379.
(91) Sancier, K. M.; Dozono, T.; Wise, H. *J. Catal.* **1971**, *23*, 270.
(92) Canadell, E.; Whangbo, M.-H.; Schelnker, C.; Escripe-Filippini, C. *Inorg. Chem.* **1989**, *28*, 1466.
(93) Zhu, Z.; Chowdhary, S.; Long, V. C.; Musfeldt, J. L.; Koo, H.-J.; Whangbo, M.-H.; Wei, X.; Negishi, H.; Inoue, M.; Sarrao, J.; Fisk, Z. *Phys. Rev. B* **2000**, *61*, 10057.
(94) *Comprehensive Handbook of Chemical Bond Energies*; Luo, Y. R., Ed.; CRC Press: Boca Raton, FL, 2003, 26.
(95) Ruscic, B.; Wagner, A. F.; Barding, L. B.; Asher, R. L.; Feller, D.; Dixon, D. A.; Peterson, K. A.; Song, Y.; Qian, X.; Ng, C.-Y.; Liu, J.; Chen, W.; Schwenke, D. W. *J. Phys. Chem. A* **2002**, *106*, 2727.
(96) Note that because the electron assigned to the metal center in the •M—O• excited state enters the conduction band and becomes spatially delocalized over the crystal lattice, there is essentially zero exchange coupling between the metal-centered and oxygen-centered electrons in the excited state. The excited state energy is therefore independent of the net spin configuration (singlet or triplet). However, the DFT calculation on the •M—O• state is substantially more straightforward in the spin triplet case, so for convenience, excited states with triplet spin configurations were used in the calculation of E_{hyb}.
(97) Stradella, L.; Vogliolo, G. *Z. Phys. Chem.* **1983**, *137*, 99.
(98) Křivánek, M.; Jírů, P.; Strnad, J. *J. Catal.* **1971**, *23*, 259.
(99) Molnar, L. F.; He, X.; Wang, B.; Merz, K. M., Jr. *J. Chem. Phys.* **2009**, *131*, 065102.
(100) Ferrighi, L.; Madsen, G. K. H.; Hammer, B. *Chem. Phys. Lett.* **2010**, *492*, 183.
(101) Madsen, G. K. H.; Ferrighi, L.; Hammer, B. *J. Phys. Chem. Lett.* **2010**, *1*, 515−519.
(102) Cao, J.; van Mourik, T. *Chem. Phys. Lett.* **2010**, *485*, 40.

(103) Sayama, K.; Nomura, A.; Arai, T.; Sugita, T.; Abe, R.; Yanagida, M.; Oi, T.; Iwasaki, Y.; Abe, Y.; Sugihara, H. *J. Phys. Chem. B* **2006**, *110*, 11352.
(104) Walsh, A.; Yan, Y.; Huda, M. N.; Al-Jassim, M. M.; Wei, S.-H. *Chem. Mater.* **2009**, *21*, 547.
(105) Stoltzfus, M. W.; Woodward, P. M.; Seshadri, R.; Klepeis, J.-H.; Bursten, B. *Inorg. Chem.* **2007**, *46*, 3839.
(106) Payne, D. J.; Robinson, M. D. M.; Egdell, R. G.; Walsh, A.; McNulty, J.; Smith, K. E.; Piper, L. F. J. *Appl. Phys. Lett.* **2011**, *98*, 212110.
(107) Zhao, Z.; Li, Z.; Zou, Z. *Phys. Chem. Chem. Phys.* **2011**, *13*, 4746.
(108) Ding, K.; Chen, B.; Fang, Z.; Zhang, Y. *Theor. Chem. Acc.* **2013**, *132*, 1352.
(109) Huang, W. L.; Zhu, Q. *J. Comput. Chem.* **2008**, *30*, 183.
(110) Payne, D. J.; Egdell, R. G.; Walsh, A.; Watson, G. W.; Guo, J.; Glans, P.-A.; Learmonth, T.; Smith, K. E. *Phys. Rev. Lett.* **2006**, *96*, 157403.
(111) Walsh, A.; Watson, W. G.; Payne, D. G.; Egdell, R. G.; Guo, J.; Glans, P.-A.; Learmonth, T.; Smith, K. E. *Phys. Rev. B* **2006**, *73*, 235104.
(112) Gao, X.; Fierro, J. L. G.; Wachs, I. E. *Langmuir* **1999**, *15*, 3169.
(113) Cuffini, S. L.; Macagno, V. A.; Carbonio, R. E.; Melo, A.; Trollund, E.; Gautier, J. L. *J. Solid State Chem.* **1993**, *105*, 161.
(114) Magalhaes, F.; Camilo Moura, F. C.; Ardisson, J. D.; Lago, R. M. *Mater. Res.* **2008**, *11*, 307.
(115) Ching, W. Y.; Mo, S.-D.; Ouyang, L.; Tanaka, I.; Yoshiya, M. *Phys. Rev. B* **2000**, *61*, 10609.
(116) Ghorpade, S. P.; Darshane, V. S.; Dixit, S. G. *Appl. Catal. A* **1998**, *166*, 135.
(117) Harunsani, M. H.; Oropeza, F. E.; Palgrave, R. G.; Egdell, R. G. *Chem. Mater.* **2010**, *22*, 1551.
(118) Pai, M. R.; Majeed, J.; Banerjee, A. M.; Arya, A.; Bhattacharya, S.; Rao, R.; Bharadwaj, S. R. *J. Phys. Chem. C* **2012**, *116*, 1458.